

See discussions, stats, and author profiles for this publication at: <https://www.researchgate.net/publication/5337858>

# Brownian Dynamics Simulations of Single-Wall Carbon Nanotube Separation by Type Using Dielectrophoresis

ARTICLE *in* THE JOURNAL OF PHYSICAL CHEMISTRY B · JULY 2008

Impact Factor: 3.3 · DOI: 10.1021/jp711450w · Source: PubMed

---

CITATIONS

16

---

READS

25

## 3 AUTHORS:



**Manuel J. Mendes**

New University of Lisbon

26 PUBLICATIONS 250 CITATIONS

SEE PROFILE



**Howard K Schmidt**

Rice University

37 PUBLICATIONS 1,291 CITATIONS

SEE PROFILE



**Matteo Pasquali**

Rice University

224 PUBLICATIONS 5,119 CITATIONS

SEE PROFILE

# Brownian Dynamics Simulations of Single-Wall Carbon Nanotube Separation by Type Using Dielectrophoresis

Manuel J. Mendes,<sup>†,‡</sup> Howard K. Schmidt,<sup>‡</sup> and Matteo Pasquali<sup>\*,‡,§</sup>

*Applied Physics Program, Department of Electrical and Computer Engineering, Carbon Nanotechnology Laboratory, Smalley Institute for Nanoscale Science and Technology, and Department of Chemical and Biomolecular Engineering, Department of Chemistry, and Computer and Information Technology Institute, Rice University, 6100 Main Street, Houston, Texas 77005*

*Received: December 4, 2007; Revised Manuscript Received: February 27, 2008*

We theoretically investigate the separation of individualized metallic and semiconducting single-wall carbon nanotubes (SWNTs) in a dielectrophoretic (DEP) flow device. The SWNT motion is simulated by a Brownian dynamics (BD) algorithm, which includes the translational and rotational effects of hydrodynamic, Brownian, dielectrophoretic, and electrophoretic forces. The device geometry is chosen to be a coaxial cylinder because it yields effective flow throughput, the DEP and flow fields are orthogonal to each other, and all the fields can be described analytically everywhere. We construct a flow-DEP phase map showing different regimes, depending on the relative magnitudes of the forces in play. The BD code is combined with an optimization algorithm that searches for the conditions that maximize the separation performance. The optimization results show that a 99% sorting performance can be achieved with typical SWNT parameters by operating in a region of the phase map where the metallic SWNTs completely orient with the field, whereas the semiconducting SWNTs partially flow-align.

## 1. Introduction

The unique characteristics of SWNTs make them potentially effective in a wide range of applications in electronics, energy, multifunctional materials, and biomedicine.

The most common techniques used in the synthesis of SWNTs are carbon arc-discharge,<sup>1</sup> laser ablation,<sup>2</sup> chemical vapor deposition,<sup>3</sup> gas-phase catalytic growth,<sup>4</sup> and catalytic decomposition on bimetallic CoMo catalysts.<sup>5</sup> As-produced nanotubes from these processes contain a broad range of  $(n, m)$  chiralities with different diameters and electronic structures.<sup>6</sup> SWNTs with  $n - m$  equal to a multiple of 3 are metallic, and the other two-thirds correspond to direct band gap semiconductors.<sup>7</sup> Whereas some applications (e.g., structural composites, fluid filtration, biomedical imaging, etc.) could be achieved with mixed-type SWNTs, others would benefit greatly from single-type (metallic vs semiconductors) or single-chirality samples (e.g., molecular electronics, field emission displays, wires for long-distance electrical power transmission, etc.).

The types of enrichment methods studied so far make use of distinct physicochemical principles: covalent functionalization,<sup>8,9</sup> selective elimination,<sup>10</sup> selective absorption,<sup>11,12</sup> ion exchange chromatography,<sup>13</sup> electrophoresis (EP),<sup>14,15</sup> dielectrophoresis (DEP)<sup>16–18,20</sup> and density gradient ultracentrifugation.<sup>22</sup> Each of these methods has a different selectivity toward type or diameter and a different potential for scaling to bulk quantities. One potentially scalable route is to couple the type of selectivity of DEP with the high-throughput provided by continuous flow devices; promising results were recently reported in ref 23.

However, flow-through DEP (FT-DEP) is characterized by a large, complex parameter space; therefore, modeling can be useful in quantifying the potential of the technique and the optimal range of operating parameters where sorting efficiency and throughput can be maximized.

The basic physics controlling DEP of rods is well-understood in terms of frequency-dependent polarizability; application of the theory to SWNTs still needs input from experimental results in terms of specific SWNT properties. Therefore, at this stage, it is prudent to analyze FT-DEP in terms of a dimensionless parameter space and, on the basis of current estimates of SWNT properties, to evaluate which regions of a FT-DEP diagram are accessible and desirable.

Here, we present a computational study of the response of individual SWNTs under positive DEP and apply it to the separation of metallic and semiconducting SWNTs with poly-disperse length in a new type of FT-DEP device with a coaxial cylindrical geometry. Earlier simulation articles studied the motion of dispersed SWNTs under the influence of DEP.<sup>20,21</sup> Here, we include the important effect of fluctuating exchange of momentum between the SWNTs and the liquid. We also combine in the algorithm a pattern search optimization method which requires no derivative information.

## 2. Dielectrophoresis on SWNTs

Dielectrophoresis is the motion of matter caused by polarization effects in a nonuniform electric field.<sup>24</sup> Consider a polarizable particle immersed in an otherwise homogeneous medium in which there exists an electric field  $\mathbf{E}$ . The interaction with the imposed field induces a dipole moment in the particle, caused by charge separation within its material. If the field is spatially nonuniform, the inclusion experiences a force imbalance, which results in its translation along the field gradient direction, even if the particle is globally uncharged. The translational DEP force

\* E-mail: mp@rice.edu

<sup>†</sup> Applied Physics Program and Department of Electrical and Computer Engineering.

<sup>‡</sup> Department of Chemical & Biomolecular Engineering and Smalley Institute for Nanoscale Science and Technology.

<sup>§</sup> Department of Chemical & Biomolecular Engineering, Department of Chemistry and Kennedy Institute for Information Technology.

is proportional to the field gradient at the particle position and to its induced dipole moment  $\mu$ .

$$\mathbf{F}^{\text{DEP}} = \mu \cdot \nabla \mathbf{E} \quad (1)$$

Because, in turn,  $\mu$  is proportional to  $\mathbf{E}$ , the DEP force is proportional to  $\nabla E^2$ . Thus, the particle DEP motion is independent of the field direction and can be driven by a DC or AC field. This effect has proven useful for nanoscale object manipulation<sup>25</sup> and separation<sup>26</sup> due to the differences in the polarizabilities of particles with distinct material properties or geometries.

Carbon nanotubes are long, thin rods, highly polarizable along the axial direction due to their pronounced shape anisotropy.<sup>27</sup> These particles are modeled as slender prolate ellipsoids to calculate analytically their induced dipole moment ( $\mu_{\text{NT}}$ ) using the Rayleigh electrostatics approximation.<sup>28</sup> This approach considers that the internal field induced inside the particle is uniform, which is valid only if the nanotube dimension is much smaller than the applied field wavelength. The wavelengths of interest for SWNT DEP separation are on the order of tens of meters (radio frequency),<sup>16–19,38</sup> which is much higher than the SWNT axial dimension ( $\sim \mu\text{m}$ ). It is also assumed that nanotubes are seen as point particles by the field gradient; that is, that their size is very small compared to the spatial change of  $\nabla E$ ,

$$|\nabla E| \gg l_{\text{NT}} |\nabla \nabla E| \quad (2)$$

where  $l_{\text{NT}}$  is the tube length. If these conditions are valid,  $\mu_{\text{NT}}$  can be determined using<sup>28,29</sup>

$$\mu_{\text{NT}} = V_{\text{NT}} \epsilon_m \mathbf{E} \cdot \mathbf{P} \quad (3)$$

where  $\mathbf{P} = \text{Re}[K^{\parallel}] \mathbf{u}\mathbf{u} + \text{Re}[K^{\perp}] (\mathbf{I} - \mathbf{u}\mathbf{u})$  is the polarizability tensor,  $\mathbf{u}$  is the unit vector along the SWNT axis,  $V_{\text{NT}}$  is the SWNT volume,  $\epsilon_m$  is the medium permittivity, and  $\text{Re}[K^{\parallel, \perp}]$  is the real parts of the radial (or perpendicular) and axial (or parallel) Clausius–Mossotti factors, which depend on the difference between the complex dielectric functions of the particle material ( $\epsilon_{\text{NT}}^*$ ) and the medium ( $\epsilon_m^*$ ),

$$K^{\perp, \parallel} = \frac{\epsilon_{\text{NT}}^* - \epsilon_m^*}{\epsilon_m^* + (\epsilon_{\text{NT}}^* - \epsilon_m^*) L^{\perp, \parallel}} \quad (4)$$

where  $L^{\perp, \parallel}$  is depolarization factors that have distinct values due to the particle shape anisotropy. In the case of long prolate ellipsoids, these factors are<sup>29</sup>

$$L^{\parallel} = \frac{4r_{\text{NT}}^2}{l_{\text{NT}}^2} \left( \log \left[ \frac{l_{\text{NT}}}{r_{\text{NT}}} \right] - 1 \right) \quad L^{\perp} = \frac{1 - L^{\parallel}}{2} \quad (5)$$

where  $r_{\text{NT}}$  is the SWNT radius. This results in a higher polarizability along the longer axis ( $\parallel$ ) of the ellipsoid.

In an AC field, the material polarization is frequency-dependent due to the energy dissipation associated with internal charge displacement. This effect is accounted for in the imaginary part of the dielectric function, which can be written in a simplified form in terms of the material optical constants, permittivity  $\epsilon$  and conductivity  $\sigma$ ,

$$\epsilon^*(\omega) = \epsilon - i \frac{\sigma}{\omega} \quad (6)$$

where  $\omega = 2\pi f$  is the AC field angular frequency.

The axial components of the SWNTs permittivity and conductivity are expected to be higher than the perpendicular ones due to the SWNT unidimensional structure.<sup>30–32</sup> However, considering this anisotropy in dielectric constants would yield

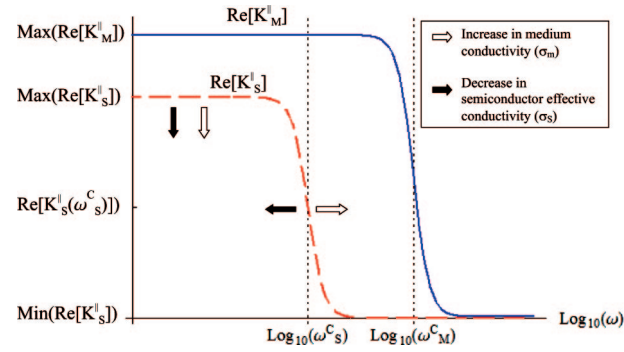


**Figure 1.** Schematic plot of the parallel Clausius–Mossotti factor for metallic (M) and semiconducting (S) SWNTs and how it changes with the surfactant effect. The main role of the surfactants is to increase the medium conductivity and reduce the effective one of wrapped SWNTs.

a negligible effect in the SWNTs' overall polarizability due to their high aspect ratio accounted for by the depolarization factors. For typical SWNT aspect ratios,  $\max(\text{Re}[K^{\parallel}]) \sim 1/L^{\parallel} \gg \max(\text{Re}[K^{\perp}]) \sim 1/L^{\perp}$ . Thus taking  $\epsilon_{\text{NT}}^*$  in  $K^{\perp}$  different from the one in  $K^{\parallel}$  would have minimal influence on the computed DEP response because the radial polarizability is negligible. Hence, SWNTs are assumed to be a homogeneous material with the same  $\epsilon_{\text{NT}}$  and  $\sigma_{\text{NT}}$  for  $K^{\parallel}$  and  $K^{\perp}$  in eq 4.

The constants  $\epsilon_{\text{NT}}$  and  $\sigma_{\text{NT}}$  are taken to be independent of  $\omega$  in the frequency range considered here for SWNT DEP separation (MHz), as described later in section V. Optical experiments on nanotube networks show that these quantities depart from their DC values only for frequencies in the THz range or higher.<sup>33–36</sup> Fits to the measured conductivity values with the Drude model yield mean scattering times on the order of  $10^{-14}$  s. Thus, the DEP sorting frequencies of interest are well below the expected SWNTs' Drude resonance.

The Clausius–Mossotti factors in eq 4 are complex quantities whose magnitude and phase are functions of  $\omega$ . The corresponding phase angle represents the phase lag between the applied field and the induced moment. Such ohmic, dispersive behavior is a consequence of the finite time required to build up charge at the particle–medium interface, due to the material finite conductivity. The characteristic buildup or decay time of charge at the nanotube surface in response to an applied field is given by the Maxwell–Wagner relaxation time constant,  $\tau$ .<sup>29</sup>

$$\tau^{\perp, \parallel} = \frac{(1 - L^{\perp, \parallel}) \epsilon_m + L^{\perp, \parallel} \epsilon_{\text{NT}}}{(1 - L^{\perp, \parallel}) \sigma_m + L^{\perp, \parallel} \sigma_{\text{NT}}} \quad \omega^C = \frac{1}{\tau^{\parallel}} \quad (7)$$

Every material has a *critical frequency*,  $\omega^C$ , above which the charge can no longer follow the alternating field switching, thereby resulting in a reduced induced dipole moment. SWNTs exhibit longitudinal polarizabilities much higher than the radial ones; therefore, the relevant critical frequency is the one associated with the axial relaxation time. Figure 1 shows a schematic plot of the real part of the parallel Clausius–Mossotti factor expected for metallic and semiconducting SWNTs as a function of  $\omega$ . This factor is constant at low frequencies but drops dramatically above  $\omega^C$  and can even reach negative values, depending on the SWNT–medium dielectric functions difference.

SWNTs in the solvent medium must be wrapped in surfactant micelles to be dispersed in liquids.<sup>37</sup> The presence of surfactants influences the medium permittivity and conductivity as well as the effective properties of the SWNT–surfactant hydrated object. Literature results showing SWNT DEP separation<sup>16–19,38</sup> reveal that the surfactant does not dominate the dielectric

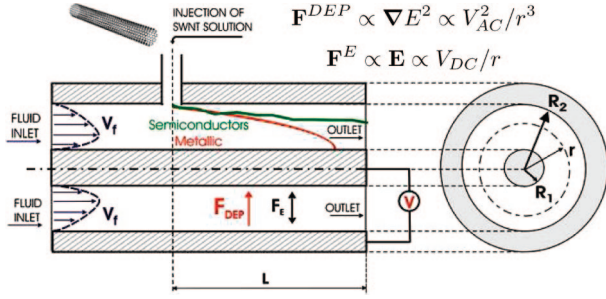


**Figure 2.** Sketch of separation device for metallic vs semiconductor separation. The dilute SWNT solution is injected at the top of the hollow cylinder. Dielectrophoretic and electrophoretic forces are generated inside the flow region using an AC voltage with a DC offset. The objective is to collect metallic SWNTs in the inner wire and let the semiconductors flow out of the device.

response of the hydrated object over the intrinsic SWNT material. Nevertheless, the surfactant effect is not negligible, and therefore,  $\epsilon_{NT}^*$  is, more correctly, the effective dielectric function of the SWNT–surfactant complex. Figure 1 shows schematically how the Clausius–Mossotti factor of a semiconductor SWNT changes due to the surfactant wrapper effect.

The  $Re[K]$  factors in the DEP force expression differ between metallic and semiconducting SWNTs since they have distinct intrinsic optical constants  $\epsilon_{NT}$  and  $\sigma_{NT}$ . Type separation is possible if  $Re[K_M]$  and  $Re[K_S]$  differ sufficiently. This motivates the definition of the polarization ratio,

$$P(\omega) = \frac{Re[K_M^{\parallel}]}{Re[K_S^{\parallel}]} \quad (8)$$

where only the parallel  $K$  factors are considered due to the SWNTs' pronounced shape anisotropy, as previously discussed. It can be seen from the plots in Figure 1 that this ratio is higher in the frequency range between the semiconductors' and metals' critical frequencies, a quantity mainly associated with the material conductivity. That is the preferential frequency window for SWNT sorting by type.

**2.A. The DEP Separation Device.** This study considers a coaxial cylindrical channel composed of an outer metallic tube and an inner metallic wire that is stretched along the cylinder axis, as depicted in Figure 2. The liquid flows between the inner wire and the tube, and a voltage is applied between them to generate an electric field within the flow region. The SWNT suspension is injected near the internal tube wall at radial position  $R_2$ .

Applying a pure AC voltage,  $V_{AC}$ , yields an inward radial DEP force, which scales as  $F^{DEP} \propto V_{AC}^2 / r^3$ , where  $r$  is the distance from the cylinder axis.

The coaxial flow channel has two advantages over the previously used interdigitated electrode array;<sup>20,23,26</sup> it is expected to perform better because, unlike the interdigitated array,  $F^{DEP}$  is always greater than zero inside the device, and it can be modeled simply because the flow and electric fields can be determined analytically if the channel length,  $L$ , is much longer than  $R_2$ .

### 3. Brownian Dynamics Algorithm

The SWNT equations of translational and rotational motion are determined using force and torque balances, in which inertia terms are ignored due to the minimal nanotube mass. The rapid process of inertia-friction relaxation of momentum occurs in

picoseconds for these particles, which is a time scale much lower than the time scales of interest.<sup>39</sup>

For simple systems with uniformly distributed fields over the whole space, the diffusive motion is best studied numerically by solving the appropriate partial differential equation for the probability distribution function in the space of possible configurations. However, in this case, the fields are spatially dependent. The system can be studied more effectively by following the trajectories of  $N$  particles; such trajectories obey stochastic differential equations, including deterministic as well as Brownian terms. Here, the stochastic equations of motion are integrated by a forward Euler scheme due to the presence of the Brownian term.

**3.A. Force Balance and Translational Motion.** The SWNT center of mass position,  $\mathbf{R}(t)$ , is displaced according to the force balance,

$$\mathbf{F}^T + \mathbf{F}^H + \mathbf{F}^B = 0 \quad (9)$$

where  $\mathbf{F}^T = \mathbf{F}^{DEP} + \mathbf{F}^{EP}$  is the total electric force that consists on the sum of DEP and electrophoretic (EP) forces. The hydrodynamic force  $\mathbf{F}^H$  is composed of two terms, a flow and a viscous force,

$$\mathbf{F}^H = \zeta \left( \mathbf{v}_f - \frac{d\mathbf{R}}{dt} \right) \quad (10)$$

where  $v_f$  is the fluid velocity and  $\zeta \equiv \zeta^{\parallel} \mathbf{u}\mathbf{u} + \zeta^{\perp} (I - \mathbf{u}\mathbf{u})$  is the friction tensor of a rigid rod.<sup>40</sup> The components of this tensor are given by  $\zeta^{\parallel} = 2\pi\eta l_{NT} / \log[l_{NT}/2r_{NT}]$  and  $\zeta^{\perp} = 2\zeta^{\parallel}$ , where  $\eta$  is the fluid viscosity. The velocity profile of a laminar incompressible fluid flow can be analytically determined in a coaxial cylindrical channel (see Figure 2) by solving the Navier–Stokes equation with the following boundary conditions:  $v_f(R_1) = 0$  and  $v_f(R_2) = 0$ .<sup>45</sup>

The Brownian force  $\mathbf{F}^B$  is a Gaussian random variable with zero mean and second moment given by a Dirac  $\delta$ -function<sup>41</sup>  $\langle \mathbf{F}^B(t') \mathbf{F}^B(t'') \rangle = 2k_B T \zeta \delta(t' - t'')$ , where  $T$  is the temperature and  $k_B$  is the Boltzmann constant. At a given time step from  $t$  to  $t + \Delta t$ , the Brownian force produces a Gaussian random displacement,  $b(t)$  of the center of mass position with zero mean and second moment,

$$\langle b(t)b(t) \rangle = 2D\Delta t \quad (11)$$

where  $D$  is the diagonal diffusivity tensor, which can be written in terms of the friction coefficient tensor:  $D = k_B T \zeta^{-1}$

Combining eqs 9–11 and discretizing the equation of motion with the forward Euler scheme yields the expression for the center of mass displacement,

$$\mathbf{R}(t + \Delta t) - \mathbf{R}(t) = \frac{\Delta t}{k_B T} D \cdot \mathbf{F}_T + \mathbf{v}_f \Delta t + b(t) \quad (12)$$

**3.B. Torque Balance and Rotational Motion.** The evolution of the unit vector  $\mathbf{u}$  aligned along the tube axis obeys a torque balance,

$$\mathbf{M}^T + \mathbf{M}^H + \mathbf{M}^B = 0 \quad (13)$$

where the indices T, H, and B refer to total electric, hydrodynamic, and Brownian torques.

The electric torque,  $M^E$ , is related to the applied field,  $E$ :

$$M^E = \mu_{NT} \times E \quad (14)$$

For the case of an AC field, the time-average of this torque over the period of the applied AC voltage is<sup>29</sup>





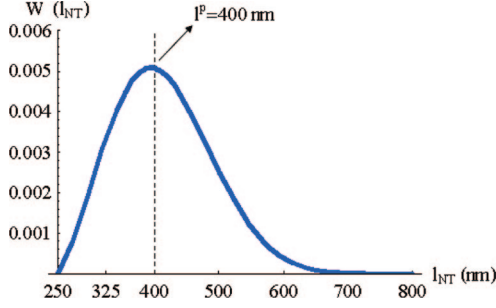


**Figure 4.** Weibull SWNT length distribution. The parameters assumed for the distribution are  $a = 6 \times 10^{-6}$ ,  $b = 2.29$ ,  $l_{\min} = 0.625l^P$ . The standard deviation is  $\sigma \approx 0.2l^P$ .

yields values on the order of  $\epsilon_S = 5\epsilon_0$ , which is consistent with the experimental observations of the authors of ref 31.<sup>31</sup> The permittivity of metallic SWNTs is expected to be higher, on the order of  $10^4\epsilon_0$ .<sup>20,21</sup>

The semiconducting SWNTs' effective conductivity,  $\sigma_S$ , can be determined by their critical frequency,  $\omega_S^C$ , using eq 7 and assuming a typical aspect ratio  $l_{NT}/r_{NT} = 800$  for as-produced HiPco nanotubes.<sup>46,47</sup> Previous studies on DEP separation<sup>16–19,38</sup> report that the semiconductors' critical frequency is on the order of  $f_S^C = 1$  MHz. Therefore, here we consider  $\omega_S^C = 2\pi f_S^C$ . These studies also reveal that the metallic tubes'  $Re[K_M^{\parallel}]$  factor remains approximately constant for frequencies around  $\omega_S^C$ , as sketched in Figure 1. Thus, here we take  $\sigma_M = 10^3\sigma_S$  for the metallic SWNTs' conductivity.

The polarization ratio,  $P(\omega)$ , becomes a function of only the field frequency, considering these material parameters. Frequencies higher than  $\omega_S^C$  and lower than the metallic SWNTs' critical frequency ( $\approx 10^3\omega_S^C$ ) allow sufficiently broad regions SB and SH, in Figure 3, for separation. As an example, a frequency of  $\omega = 3\omega_S^C$  yields 1 order of magnitude difference between the metallic and semiconducting SWNTs' polarizability ( $P(\omega) \approx 10$ ).

The particular SWNT material constants taken from literature depend on the surfactant and medium conditions used. Therefore, in this work, the simulation results are given in terms of the dimensionless  $P(\omega)$  values.

**4.A. SWNT Dimensions.** The statistics of HiPco-generated SWNT lengths have been studied using AFM imaging, and the Weibull distribution function ( $W$ ) was shown to have the best fit to the measured length histograms.<sup>46</sup> The general expression for this distribution is

$$W(l) = ab(l - l_{\min})^{b-1}e^{-a(l-l_{\min})^b} \quad l > l_{\min} \quad (20)$$

where  $a$  and  $b$  are the scale and shape parameters, and  $l_{\min}$  is the minimum length considered.

All the forces and torques listed in eqs 9 and 13 are length-dependent, so broad distributions make sorting harder. Typical HiPco SWNT length distributions<sup>46,47</sup> range from  $l_{\min} \approx 0$  to a few micrometers. However, recent length separation studies<sup>48,49</sup> have shown that short nanotubes can be removed in a feasible way up to a significant minimum length, achieving narrower distributions devoid of short SWNTs. These distributions are preferred for type separation; therefore, in this work, the length  $l_{NT}$  of each SWNT is generated through a random number following a length-sorted distribution depicted in Figure 4.

All SWNTs are taken to have the same fixed radius,  $r_{NT} = l^P/800$ , where  $l^P$  is the Weibull distribution peak length.

Particularly the Clausius–Mossotti factor is very sensitive to the rod aspect ratio  $l_{NT}/r_{NT}$ , as depicted in the plots of Figure

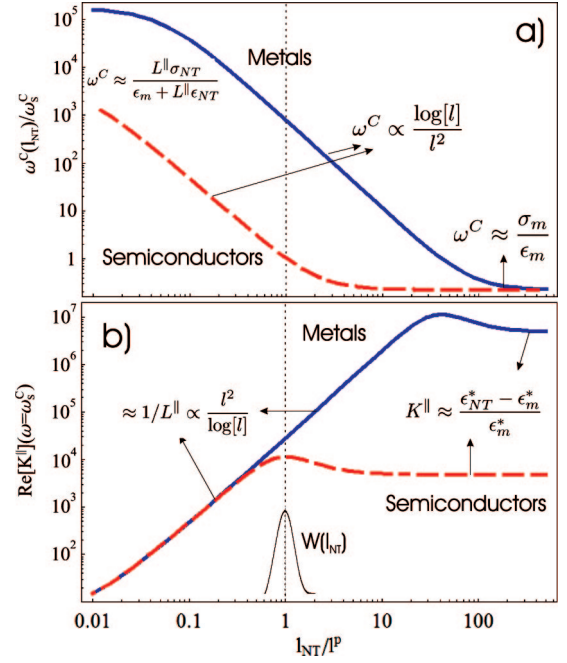


**Figure 5.** (a) Critical frequency,  $\omega^C$ , in units of  $\omega_S^C$  as a function of the SWNT length  $l_{NT}$  in units of  $l^P$ . (b) Real part of the parallel Clausius–Mossotti factor as a function of length at the semiconductors' critical frequencies,  $\omega_S^C$ . The curve  $W(l)$  corresponds to our length distribution in Figure 4. Both quantities are shown for metals (blue) and semiconductors (red).

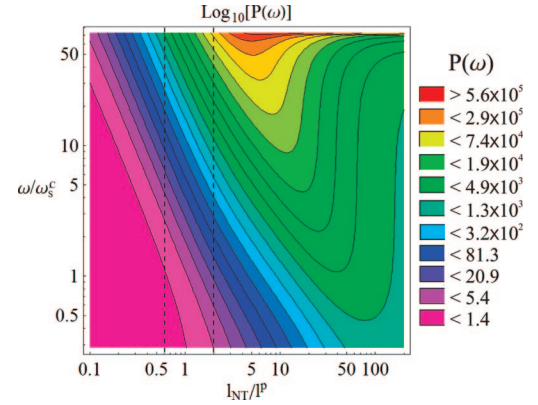


**Figure 6.** Color contour plot of the polarization ratio,  $P(\omega)$  (in logarithmic scale), as a function of frequency,  $\omega$  (in units of  $\omega_S^C$ ), and the SWNT length,  $l_{NT}$  (in units of  $l^P$ ). The region inside the dashed lines corresponds to the length distribution in Figure 4.

5. Figure 5a shows that the critical frequency  $\omega^C$  decreases monotonically with length because it takes more time for charge buildup at the SWNT/medium interfaces (eq 7). The critical frequency ( $\omega_S^C$ ) of the semiconductors is taken to be the critical frequency of a SWNT whose length is  $l^P$ . Figure 5b shows how the  $Re[K^{\parallel}]$  factor changes with length at that frequency,  $\omega_S^C$ . For low-aspect ratios, the induced dipole moment  $\mu_{NT}$ , given in eq 3, scales with  $l_{NT}^3/\log(l_{NT})$ ; for high lengths, it just increases proportionally to the volume ( $V_{NT}$ ) because  $Re[K^{\parallel}]$  becomes length-independent.

The contour plot of Figure 6 depicts the logarithm of the polarization ratio,  $P(\omega)$ , as a function of the frequency and SWNT length. The dashed vertical lines represent the limits of the length distribution in Figure 4. The ratio of the curves in Figure 5b corresponds here to  $\omega/\omega_S^C = 1$ . The length at which those curves split corresponds approximately to the minimum

length considered for this study ( $l_{\min}$ ) so that the Weibull distribution lies in a favorable region for separation:  $P(\omega_S^C, l_{\min}) \geq 1.4$ , as shown in Figure 6.

For simplicity, when referring to the polarization ratio  $P(\omega)$  in the following sections of this paper, it is the one corresponding to the peak length,  $l_{NT} = l^p$ , unless stated otherwise.

**4.B. Initial Separation Conditions.** The initial device conditions shall be chosen by setting the following dimensionless ratios relative to a metallic SWNT with length  $l^p$ .

$$\frac{R_2}{l^p} = 10^3 \quad (21)$$

$$\frac{U_R^{\text{DEP}}(R_2)}{k_B T} = 10 \quad (22)$$

$$\frac{T^{\text{DEP}}(R_2 \rightarrow R_1)}{T^{\text{BM}}(R_2 \rightarrow R_1)} = 0.1 \quad (23)$$

$$Pe(R_1) = \frac{\partial v_f}{\partial r} \Big|_{R_1} = 0.01 \quad (24)$$

$U_R^{\text{DEP}}(R_2)$  is the rotational DEP energy (equal to the maximum torque magnitude) at  $R_2$ .  $T^{\text{DEP}}(R_2 \rightarrow R_1)$  is the analytically calculated transit time for a SWNT aligned with the field lines to cross the channel radially with just the DEP and viscous force ( $F_{\text{DEP}}^{\parallel}(r) = \zeta^{\parallel} dr/dt$ ). This time interval is given by

$$T^{\text{DEP}}(r_i \rightarrow r_f) = \frac{\zeta^{\parallel}(r_i^4 - r_f^4)}{4V_{\text{NT}}\epsilon_m Re[K_M^{\parallel}] \left( \frac{\log[R_2/R_1]}{V_{AC}/\sqrt{2}} \right)^2} \quad (25)$$

$T^{\text{BM}}(R_2 \rightarrow R_1)$  is the time to randomly diffuse a distance,  $d = R_2 - R_1$ , obtained with the Einstein diffusion equation:  $d^2 = 6Dt$ . The inverse of the dimensionless number in eq 23 is the ratio of the average DEP velocity over diffusion.

The last ratio (eq 24) is the Peclet number ( $Pe$ ) at the position of highest shear, which relates the flow and Brownian torque. With such a low  $Pe$ , shear cannot overcome Brownian motion to cause flow alignment. In this case, the magnitude of the DEP torque on metals (eq 15) versus the flow torque (eq 16) is  $M_M^{\text{DEP}}/M^F = 1551.28$  at  $R_2$ .

At the channel entrance ( $r = R_2$ ), our system is placed in the preferential regime SB of Figure 3 using the parameters in eqs 21–24, provided that  $P(\omega) \geq 10$ .

**IVC. Simulation Conditions.** The Brownian dynamics algorithm was implemented in Fortran 90 code using Message Passing Interface (MPI) for parallel computation on distributed memory systems (typically 20–100 processors). The Rice ADA Cray cluster was the computational environment used to run the programs. It is a 632 AMD64 CPU core machine with dual core CPUs and rapid array interconnect. Each CPU is a 2.2 GHz AMD Opteron with 1 MB L2 cache.

Every simulation was performed using 9000 SWNTs, of which 3000 were metallic and 6000 were semiconductors, to mimic equidistribution of SWNT chiralities ( $n, m$ ). This is statistically a sufficiently high number of particles for all the calculations, as discussed in Section 6B, below.

The time step used was always chosen to be less than the maximum time step allowed for the integration of a metallic tube's rotational motion, calculated using eq 19.

## 5. Results Using only DEP

A convenient natural time unit to use in the analysis of the SWNTs' translational motion is the analytically calculated transit

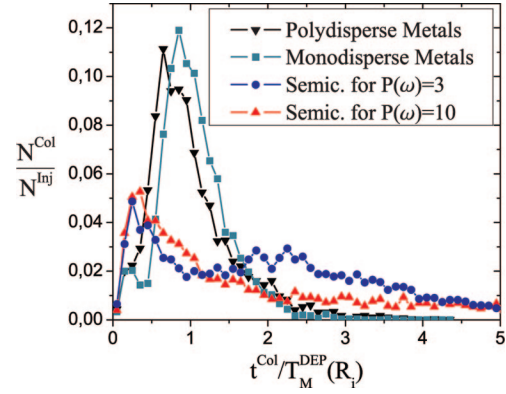


**Figure 7.** Histograms of the number of collected SWNTs,  $N^{\text{col}}$ , normalized by the corresponding number of injected tubes,  $N^{\text{inj}}$ , as a function of the transit or collection time,  $t^{\text{col}}$ , in units of  $T_M^{\text{DEP}}(R_i)$ . Results are shown for metallic tubes with polydisperse Weibull lengths and with a monodisperse length equal to the Weibull distribution peak  $l_{NT} = l^p$ . The behavior of polydisperse-length semiconductors is shown for  $P(\omega) = 3$  and  $P(\omega) = 10$ . For both polarization ratios, the behavior of the metallic tubes is the same. The peak at  $t^{\text{col}}/T_M^{\text{DEP}}(R_i) \approx 0.3$  for semiconductors corresponds to the tubes that diffused from  $R_i$  to the outer wall at  $R_2$ .

time for a metallic tube, of length  $l^p$  and aligned with the field lines, to go from the injection point,  $R_i$ , to the inner wire,  $R_1$  ( $T_M^{\text{DEP}}(R_i)$ ), determined with eq 25.

The simulation runs until all metallic tubes are collected; the transit or collection time  $t^{\text{col}}$  is recorded. Figure 7 displays the number of collected SWNTs ( $N^{\text{col}}$ ) as a function of  $t^{\text{col}}$  in units of  $T_M^{\text{DEP}}(R_i)$ . For both polarization ratios,  $P(\omega)$ , shown in the graphic, the behavior of the metallic tubes is the same because this would correspond to changing the frequency next to  $\omega_S^C$ , where the Clausius–Mossotti factor on metals remains invariant.

The histogram of polydisperse-length metallic tubes is compared with the one of a monodisperse length  $l_{NT} = l^p$  population. The polydisperse peak is shifted left relative to the monodisperse due to the Weibull distribution right skewness. This yields slightly more tubes with  $l_{NT} > l^p$ , which implies a higher average DEP force, since the induced dipole moment on metallic SWNTs scales with  $l_{NT}^3/\log(l_{NT})$  (see Section 4A).

For  $P(\omega) = 10$ , the DEP energy on semiconducting SWNTs is low. The ratio in eq 22 gives  $U_R^{\text{DEP}}(R_2)/k_B T = 0.9$  for semiconductors, which positions them in the Brownian regime of the phase map in Figure 3. That explains the existence of a single semiconductor collection peak at  $t^{\text{col}}/T_M^{\text{DEP}}(R_i) \approx 0.3$ , which corresponds to the tubes that just diffuse from the injection point to the outer cylinder wall at  $R_2$ . For  $P(\omega) = 3$ , this diffusion peak is also present; however, there is also collection at  $R_1$  corresponding to the small peaks at  $t^{\text{col}} > T_M^{\text{DEP}}(R_i)$ .

To quantify the degree of separation, we used two normalized quantities:<sup>20</sup>

- Separation efficiency ( $\alpha$ ). This quantity is dependent on mainly the collection of metallic SWNTs. It is 1 if all metallic tubes have been collected and there are still some semiconductors left in solution:

$$\alpha = \frac{N_S^{\text{sol}}}{N_S^{\text{sol}} + N_M^{\text{sol}}} \quad (26)$$

where the superscript sol denotes SWNTs left in solution (not collected).



- Yield of semiconductors ( $Y$ ). Fraction of semiconducting SWNTs that remain dispersed and exit the device:

$$Y = \frac{N_S^{\text{sol}}}{N_S^{\text{inj}}} \quad (27)$$

The ideal situation occurs when both of these ratios are equal to 1, meaning that all metallic SWNTs were collected and all semiconductors remained in solution.  $\alpha$  and  $Y$  do not change considerably for polarization ratios  $P(\omega) > 10$  because the dimensionless parameters listed in Section 4B were chosen so that semiconducting SWNTs with polarizability at least 1 order of magnitude lower than the one of metallic tubes have almost no DEP response (regime SB of phase diagram in Figure 3).

Figure 7 shows that practically all metallic SWNTs are collected before  $3T_M^{\text{DEP}}(R_2)$ . At that time,  $\alpha$  reaches unity, but the yield is poor ( $Y < 40\%$ ) because a significant percentage of the semiconductors diffuse to  $R_2$  and are collected before the metals.

If the SWNTs are stabilized by ionic surfactants, this diffusion problem can be eliminated by using an additional small electrophoretic (EP) force that acts on the charged surfactant micelles of both SWNT species and forces the semiconductors to remain in solution, pushing them away from the top electrode.

## 6. Separation with Dielectrophoresis (DEP) and Electrophoresis (EP)

**6.A. Electrophoresis on SWNTs.** An EP force,  $F^E$ , can be added to the DEP force by adding a DC offset,  $V_{\text{DC}}$ , to the AC voltage. This force is proportional to the net charge on the nanotubes,  $q_{\text{NT}}$  and to the DC electric field,  $E^{\text{DC}}$ , generated by the offset voltage.

$$\mathbf{F}^E(r) = q_{\text{NT}} \mathbf{E}_{\text{DC}}(\mathbf{r}) = \frac{q_{\text{NT}} V_{\text{DC}}}{\log[R_2/R_1]} \frac{\mathbf{r}}{r} \quad (28)$$

The SWNTs' net charge comes from the ionic surfactant molecules wrapped around their surface.<sup>14,15</sup> Therefore, this force is taken to act equally on metallic and semiconducting tubes because there is no type-selective attachment between the surfactants and the SWNTs.

The EP force can considerably increase the amount of semiconductors that remains in the flow region; improving the output yield,  $Y$ . For that purpose, the DC positive electrode must be applied to the inner wire (for negatively charged surfactants) so that  $\mathbf{F}^E$  points inward (like  $\mathbf{F}^{\text{DEP}}$ ).

The value of  $q_{\text{NT}}$  for a certain tube depends on the type of surfactant and should be proportional to the nanotube length,  $l_{\text{NT}}$ , assuming a fixed diameter for all SWNTs. Therefore, the product  $q_{\text{NT}} V_{\text{DC}}$  in eq 28 is treated as a single variable which obeys

$$q_{\text{NT}} V_{\text{DC}} = C_q l_{\text{NT}} \quad (29)$$

The constant of proportionality,  $C_q$ , is initially fixed by taking the DEP and EP forces on a metallic SWNT with  $l_{\text{NT}} = l^p$  to be equal at  $R_2$ :

$$\frac{F_M^{\text{DEP}}(R_2)}{F^E(R_2)} = 1 \quad (30)$$

$F^{\text{DEP}}$  scales with  $1/r^3$ , and  $F^E$  scales with  $1/r$ ; thus, condition 30 ensures that the highest possible EP force is used without overcoming DEP anywhere inside the flow region. In this way, adding electrophoresis only increases the semiconductor yield without reducing the separation efficiency.

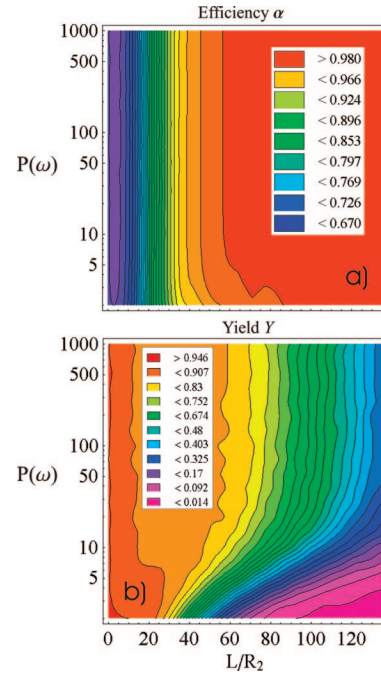


**Figure 8.** (a) Contour plot of the efficiency  $\alpha$  (which means the collection of metallic SWNTs) as a function of the channel aspect ratio,  $L/R_2$ , and polarization ratio,  $P(\omega)$ . (b) Contour plot of yield,  $Y$  (which means the amount of semiconducting SWNTs that remain in the flow). All SWNT samples obey a Weibull length distribution.

**6.B. Results with DEP and EP.** The quantities  $\alpha$  and  $Y$  were calculated as a function of the channel length and polarization ratio using the dimensionless parameters in Section 4B and the additional electrophoretic force previously introduced.

Figure 8a shows that the sorting efficiency,  $\alpha$ , is almost independent of  $P(\omega)$ . For sufficiently long channels, all metallic SWNTs are collected on the inner wire.

Figure 8b shows the yield,  $Y$ . This quantity depends strongly on  $P(\omega)$  because it is a function of the amount of semiconducting SWNTs that stay dispersed in solution. Excessively long channels lead to a lower  $Y$  as more semiconductors get collected.

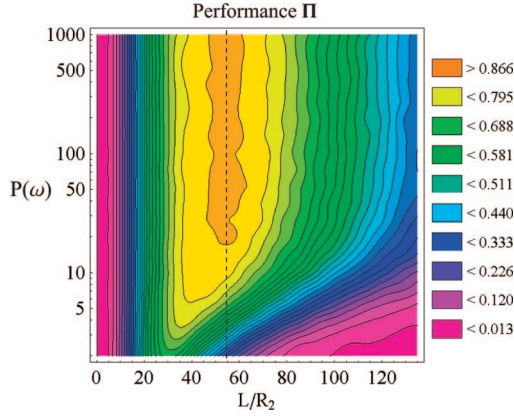
The analysis of these contour plots reveals that  $L/R_2$  should be sufficiently high for good efficiency, but at the same time, it must be low enough to achieve a reasonable yield. To determine the best channel length, we define the performance.

$$\Pi = \frac{N_M^{\text{col}} N_S^{\text{sol}}}{N_M^{\text{inj}} N_S^{\text{inj}}} \quad (31)$$

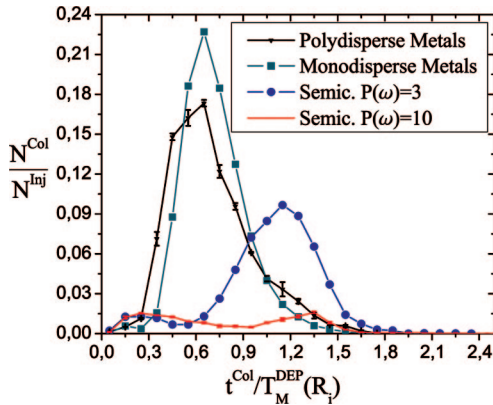
This ratio gives a quantity that is similar to the efficiency multiplied by the yield, but is also independent of the initial fraction of injected semiconductors versus injected metals. The performance contour plot is shown in Figure 9. The region of highest  $\Pi$  is the band centered around the optimal channel aspect ratio  $L/R_2(\text{opt}) = 54.2$ . Moreover, the performance becomes nearly independent of the polarization ratio when  $P(\omega) \gtrsim 10$ , because that is the threshold above which semiconducting SWNTs cease to exhibit a significant DEP response.

Figure 10 depicts the number of collected SWNTs as a function of the collection time, using  $L/R_2(\text{opt}) = 54.2$ . This graph can be compared with Figure 7, which shows the same histograms for DEP-only separation. The additional EP force reduces substantially the semiconductor collection peak corresponding to diffusion to the outer wall at  $R_2$ , that is, a greater portion of the semiconducting SWNTs remain in the flow, and





**Figure 9.** Performance  $\Pi$  contour plot. This quantity is similar to the efficiency multiplied by the yield but also independent of the initial fraction of injected semiconductors versus injected metals. The vertical dashed line marks the best channel length at  $L/R_2(\text{opt}) = 54.2$ .



**Figure 10.** Histograms of the number of collected SWNTs,  $N^{\text{col}}$ , divided by the corresponding number of injected tubes,  $N^{\text{inj}}$ , as a function of the transit or collection time,  $t^{\text{col}}$ , in units of  $T_M^{\text{DEP}}(R_1)$ . Results are shown for polydisperse- (with the distribution in Figure 4) and monodisperse- ( $l_{\text{NT}} = l^p$ ) length metallic tubes. The collection of polydisperse semiconductors is shown for  $P(\omega) = 3$  and  $P(\omega) = 10$ . Error bars are present in the histogram points for polydisperse metals and semiconductors with  $P(\omega) = 10$ . Comparing with Figure 7, we can see that the peak that was at  $t^{\text{col}}/T_M^{\text{DEP}}(R_1) \approx 0.3$ , for semiconductors which diffused to  $R_2$ , practically disappears due to the additional EP force.

the yields are substantially higher. Moreover, the device performs faster; the monodisperse metallic SWNT peak is now at  $t^{\text{col}} \approx 0.7T_M^{\text{DEP}}(R_1)$ , whereas in the case of DEP alone, the peak collection was at  $T_M^{\text{DEP}}(R_1)$ .

To confirm that the ensemble size (3000 metals + 6000 semiconductors) used for the simulations is large enough, error bars corresponding to polydisperse-length metals and semiconducting SWNTs with  $P(\omega) = 10$  were computed for the curves in Figure 10. These errors were calculated by running two simulations for each case, with distinct random number seeds in every processor, and then calculating the absolute value of the difference between the quantities given by both trials. For the  $P(\omega) = 10$  semiconductor curve, the error bars are so small that they can barely be distinguished, and for the polydisperse metallic SWNTs, they are less than 10% of the mean.

Figure 11 shows the average tube orientation relative to the radial direction,  $\mathbf{r}$ , as a function of time. Metallic SWNTs quickly align with the field direction, whereas semiconductors remain more randomly oriented at frequencies close to the critical one, as expected from the diagram in Figure 3. The same

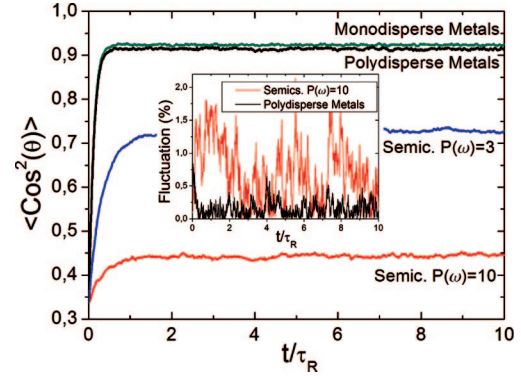


**Figure 11.** Average SWNT orientation for polydisperse- and monodisperse-length metallic tubes and polydisperse semiconductors using  $P(\omega) = 3$  and  $P(\omega) = 10$ .  $\theta$  is the angle between the nanotube direction,  $\mathbf{u}$ , and the field direction,  $\mathbf{r}$ . The inset shows the percentage difference between the results of two simulations with distinct random numbers. The time unit used here is the rotational diffusion relaxation time,  $\tau_R = 1/2D^R$  for a tube with  $l_{\text{NT}} = l^p$ .

**TABLE 1: Optimal Operational Conditions Calculated by the Nelder and Mead Direct Search Algorithm Using  $P(\omega) = 10^a$**

| dimensionless quantity   | (a) polydisperse<br>Weibull length <sup>a</sup> $W(l)$ | (b) bidisperse<br>length <sup>b</sup> ( $l^p$ and $l^p/5$ ) |
|--|--|---|
| $R_2/l^p$  | 587.5  | 477.5   |
| $[U_R^{\text{DEP}}(R_2)]/(k_B T)$  | 118.9  | 187.02  |
| $[T^{\text{DEP}}(R_2 \rightarrow R_1)]/[T^{\text{BM}}(R_2 \rightarrow R_1)]$ | $9.42 \times 10^{-3}$                                  | $6.11 \times 10^{-3}$                                       |
| $Pe(R_1)$  | 18.13  | 28.97   |
| $[FM^{\text{DEP}}(R_2)]/[E(R_2)]$  | 10.9   | 23.7  |
| $L/R_2$  | 4765.96  | 6157.07   |
| performance $\Pi$  | 0.991  | 0.562   |

<sup>a</sup> These dimensionless numbers were defined in Section 4B. Column a: Using these conditions, almost total metallic vs semiconducting SWNT separation is achieved for polydisperse-length SWNTs. Column b: In this bidisperse case, the maximum  $\Pi$  that can be obtained is 0.5625.

was observed by the authors of ref 19 in a recent contribution. The orientation fluctuations shown in the inset are below 2%, which indicates that the total number of particles used is large enough for both metals and semiconductors.

## 7. Nelder and Mead Optimization Algorithm

Conditions mentioned in Section 4B, together with the optimal channel aspect ratio calculated in the previous section, yield a performance of about 83% for  $P(\omega) = 10$ ; however, these conditions can be tuned to improve the sorting.

To find the overall maximum performance,  $\Pi$ , we make use of a multidimensional direct search algorithm known as the Nelder and Mead or downhill simplex method.<sup>51,52</sup> This method has found widespread use in the optimization of nonlinear functions whose gradient is very expensive (or practically impossible) to calculate. It has also been shown to work well for stochastic problems, as in the present case where we want to determine the set of six dimensionless numbers, listed in the first column of table 1, that maximize the performance function  $\Pi$ . These six quantities can be treated as the coordinates of a six-dimensional space in which  $\Pi$  is defined.

The basic notion behind the Nelder and Mead technique for maximizing (or minimizing) a function with  $n$  variables is to pick  $n + 1$  starting points, at which the function is evaluated, forming an  $n$ -simplex (an  $n$ -dimensional analogue of a triangle). The procedure then iteratively moves and redimensions the

simplex along the coordinate space as better points are found until some desired bound is obtained.

The range of each variable is restricted to avoid searching in physically forbidden regions or where it is known a priori that the performance is going to be low. The two most crucial physical limits are the following:

- The flow regime must be laminar; that is, the Reynolds number should be  $Re < 1000$ , and
- The channel must be much larger than the SWNTs ( $R_1/l_p > 10$  and  $(R_2 - R_1)/l_p > 100$ ) for the condition in eq 2 to be verified.

These boundaries set an upper limit to the SH separation regime in the phase portrait of Figure 3. Lower and upper bounds are assigned to each coordinate in the six-dimensional space. To restrict the searching direction inside our chosen domain, the maximizing function is set to a low value at any point outside the allowed region so that out-of-bounds points are not considered for the new simplex in the next iteration.

The search for the global performance maximum, within the defined six-dimensional domain, can be made substantially faster with a good choice of the initial seven-point simplex. This initial simplex must be nondegenerate; that is, its 6D volume cannot be zero, and it should cover a significant portion of the total domain volume. Therefore, six of the initial simplex vertices are set close to different domain boundaries. The seventh point is set with the previous parameters used in the simulations of Section 6B, which places our system in the SB regime of Figure 3. These conditions constitute a good initial guess for our searching direction, which causes the simplex to shrink in the first iterations toward the seventh point. Afterward, it reflects and expands toward regions of higher  $\Pi$  until it shrinks to a single point at the peak performance found. A minimal polarization ratio,  $P(\omega) = 10$ , is taken for the optimization because significant differences are not expected for higher  $P(\omega)$ , according to Figure 9.

The algorithm is able to reach a maximum within about 60 iterations. However, generally, this is a local maximum in the search domain. To find the global performance maximum, the Nelder and Mead program is sequentially run with different initial seven-point sets that include the previously obtained local maxima. Finally, the algorithm reaches the absolute peak performance with the dimensionless values shown in Table 1.

For polydisperse-length SWNTs, the conditions in column a of Table 1 result in almost total collection of metallic tubes with no collection of semiconductors. Interestingly, the optimization algorithm converges to points with higher  $Pe$  numbers than the one initially used (given by eq 24). With the quantities in column a of Table 1, the magnitude of the SWNT DEP torque (eq 15) versus the flow torque (eq 16) is  $M_M^{\text{DEP}}/M^F = 9.68$  for a metallic nanotube with length  $l_p$  at  $R_2$ , whereas for a semiconductor, it is  $M_S^{\text{DEP}}/M^F = 0.88$ . Therefore, near the outer wall of the device, the optimized system is in region SH of the phase diagram in Figure 3. The SH regime is expected to yield higher performance than the SB, since the semiconductors' DEP response is substantially reduced upon flow alignment. Another advantage of using a higher  $Pe$  is that it enables a larger flow rate of separated SWNTs; a higher main flow allows a higher injection flow, as discussed in Appendix A; that is, a higher throughput.

Column b of table 1 shows the results of a simulation using an equal number of SWNTs of just two lengths ( $l_p$  and  $l_p/5$ ) to mimic the effect of a sample in which the short SWNTs have not been removed. The graphics in Figures 5b and 6 indicate that for  $l_{\text{NT}} = l_p/5$ , the semiconducting and metallic SWNT DEP

response should be very similar at frequencies on the order of  $\omega_S^C$ . Therefore, if one metallic  $l_p/5$  tube is collected, then two semiconducting  $l_p/5$  tubes should also be collected, because each simulation has twice the number of semiconductors ( $N_S^{\text{inj}} = 2N_M^{\text{inj}}$ ). Under these conditions, the performance is badly degraded, and the maximum achievable value is  $\Pi = 0.5625$ .

Nevertheless, even if short SWNTs are present, good separation can still be achieved by using higher frequencies. The contour plot in Figure 6 shows that a polarization ratio  $P(\omega, l_p/5) \approx 10$  is obtained for  $l_p/5$  tubes at a frequency of  $\omega = 45\omega_S^C$ . The bidisperse case optimization was repeated with these conditions, and a high peak separation performance,  $\Pi = 0.998$ , was achieved, as expected.

## 8. Conclusions

A novel DEP separation device using a coaxial cylindrical geometry is studied theoretically in this work.

The different regimes that characterize the behavior of metallic and semiconducting SWNTs in a flow-DEP device are analyzed. Two preferential regimes for separation between the SWNT types are identified. A set of dimensionless conditions is given that place the system in the first regime, SB, where the metallic SWNTs' motion is DEP-dominated, and the semiconductors' motion is diffusive. The expected behavior of both SWNT types is confirmed with the numerical results presented. Moreover, it is shown that the sorted SWNT yield can be substantially increased by adding an electrophoretic force acting on the charged surfactant micelles.

A direct search optimization algorithm to obtain the parameters that maximize the separation performance is implemented. The algorithm shows that optimal separation is achieved in the regime SH, where the semiconducting SWNTs align with the flow, whereas the metallic SWNTs orient with the field. We examine the effect of short SWNTs, and we find that at fixed frequency, short SWNTs can degrade performance significantly; however, they can be separated successfully by raising the DEP frequency to establish a sufficiently large polarization ratio for the shorter SWNTs.

This work will be useful in developing experimental devices for continuous flow-DEP separation of SWNTs. The results provided in dimensionless form allow the optimization for distinct experimental conditions and also the possible incorporation of corrections in the model physical parameters due to additional effects not considered here.

## Appendix A

**Analysis of SWNT Starting Condition.** In this section, the SWNT starting condition is modeled considering that the nanotube solution is injected with a flow,  $Q_{\text{inj}}$ , from an aperture at the cylinder wall into the solvent flow,  $Q$  (illustrated in Figure 12).

The position of the separation surface between the two converging flows can be determined by assuming the following conditions:<sup>53</sup>

- Both inlet and main flows are fully developed and steady,
- Fluids are perfectly miscible,
- The inlet and outlet have the same geometrical shape (circular), and
- Injection flow inertia is sufficiently small; that is, the Reynolds number,  $Re^{\text{inj}}$  is  $\leq 10$ .

If these conditions are verified, the interface can be taken as a planar surface at a position  $h$ , calculated by the requirement:

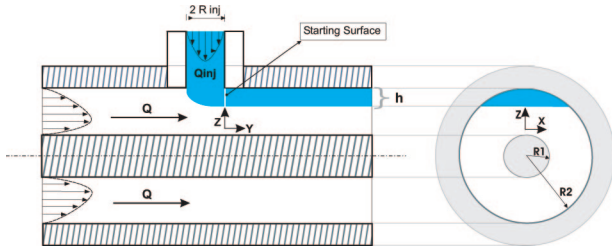


**Figure 12.** Sketch of the planar layer boundary between the injection and main flow at  $z = R_2 - h$ . It is assumed that the injection Reynolds number,  $Re^{inj}$ , is  $\leq 10$ .

$$\frac{Q_{inj}}{Q_T} = \frac{\int_{R_2-h}^{R_2} \int_0^{\sqrt{R_2-z^2}} v_f(x, z) dx dz}{\int_0^{R_2} \int_0^{\sqrt{R_2-z^2}} v_f(x, z) dx dz} \quad (A1)$$

where  $v_f(x, z)$  is the fully developed velocity profile inside the main hollow tube, and  $Q_T = Q + Q_{inj}$  is the total volumetric flow rate in the main stream after the injection. The integration is performed in Cartesian coordinates, since the interface is located at  $z = R_2 - h$ , as depicted in Figure 12.

The flow coming from the inlet becomes fully developed within a few channel diameters downstream of the junction if the injection Reynolds number,  $Re^{inj}$  is on the order of 1.

The separation layer position,  $h$ , depends mainly on the flow ratio  $Q_T/Q_{inj}$ . For the initial conditions considered in this article, given by the ratios in Section 7, a 2 orders of magnitude difference between the flows yields:

$$\frac{Q_T}{Q_{inj}} = 100 \Rightarrow h = 0.128R_2 \quad (A2)$$

The SWNTs' initial positions are now taken as random numbers located in a cross-sectional area of the channel, at  $y = 0$ , between  $z = R_2 - h$  and  $z = R_2$ . The probability,  $p$ , for a nanotube to be at a position  $(x, z)$  in that starting semicircle should be proportional to the fluid velocity at that point,

$$p(x, x+dx; z, z+dz) = C v_f(x, z) dx dz \quad (A3)$$

where  $C$  is a normalization constant given by the inverse of  $Q_{inj}$ .

The symmetry of  $v_f$  in  $x$  allows us to simplify the probability distribution to a single variable by integrating  $p(x, z)$  over the  $x$  domain. This yields the contracted distribution function  $f(z)$ :

$$f(z, z+dz) = 2 \int_0^{\sqrt{R_2-z^2}} p(x, x+dx; z, z+dz) \quad (A4)$$

which corresponds to the probability of finding a nanotube at a position  $z$  within the starting surface. The associated cumulative distribution function ( $F(z)$ ) is obtained by integrating eq 35 from  $R_2-h$  to  $z$ . The inverse function of  $F(z)$ ,  $G(\Gamma)$ , outputs the  $z$  value that corresponds to a certain cumulative probability,  $\Gamma$ . The position of 50% probability is at  $\bar{z}_i = G(0.5) = 0.905R_2$ , and this corresponds to a mean value for the SWNTs' starting location.

In the simulations performed throughout the paper, it is assumed that the SWNTs initiate their motion at  $R_i = 0.9R_2$ , which matches the mean starting position  $\bar{z}_i$  for a flow ratio  $Q_T/Q_{inj} = 100$ . In order to test the validity of single point injection at  $R_i = G(0.5)$ , two of the curves in Figure 10 are compared in Figure 13 with the corresponding histograms using nanotubes initiated at random  $z$  positions within the starting surface (following distribution in eq A4).

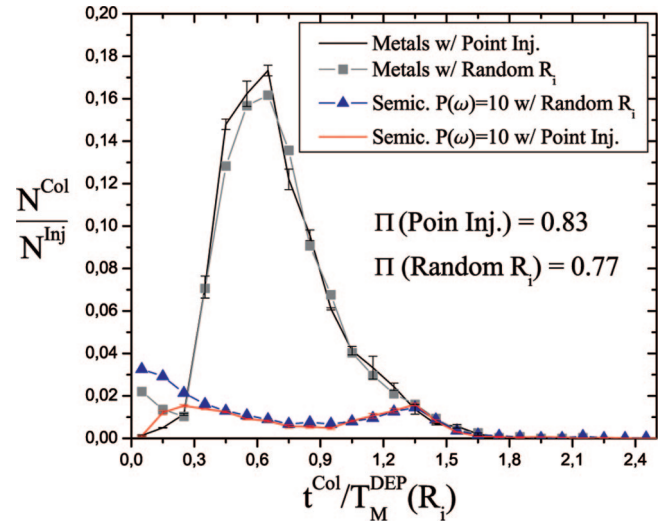


**Figure 13.** Comparison between the SWNT collection histograms of Figure 10, assuming point injection and the ones with a random initial position in  $z$  inside the starting surface. Only one polarization ratio,  $P(\omega) = 10$ , is considered, for polydisperse-length tubes. Using a flow ratio  $Q_T/Q_{inj} = 100$ , there is a decrease of 0.06 in the performance of the device relative to single-point injection.

There is a slight distinction at the beginning of motion between the general case of random  $R_i$  and the assumption of point injection at  $R_i = G(0.5)$ , as shown in Figure 13. This is because in the random  $R_i$  case, the small SWNT fraction initiated close to  $R_2$  has a higher probability of sticking to the outer cylinder wall. This effect is more significant in the semiconducting SWNTs' motion and results in a discrepancy of 0.06 in the calculated device performance.

**Acknowledgment.** We gratefully acknowledge support for this work from the National Aeronautics and Space Administration under the Houston Advanced Research Center (NNJ06H125A) and from Texas Emerging Technology Fund (ETF 07082301). Computational resources were provided by the Rice Terascale Cluster funded by NSF (EIA-0216467), Intel, and HewlettPackard, and the Rice Cray XD1 Research Cluster funded by NSF (CNS-0421109), AMD, and Cray. We thank Noe Alvarez, Dvir Kafri, Seth Marvel, Prof. Robert Hauge, and Prof. James Tour for their help.

## References and Notes

- (1) Ebbesen, T. W.; Ajayan, P. M. *Nature* **1992**, 358, 220.
- (2) Thess, A.; Lee, R.; Nikolaev, P.; Dai, H.; Petit, P.; Robert, J.; Xu, C.; Lee, Y. H.; Kim, S. G.; Rinzler, A. G.; Colbert, D. T.; Scuseria, G. E.; Tománek, D.; Fischer, J. E.; Smalley, R. E. *Science* **1996**, 273, 483.
- (3) Cheng, H. M.; Li, F.; Su, G.; Pan, H. Y.; He, L. L.; Sun, X.; Dresselhaus, M. S. *Appl. Phys. Lett.* **1998**, 72, 3282.
- (4) Nikolaev, P.; Bronikowski, M. J.; Bradley, R. K.; Rohmund, F.; Colbert, D. T.; Smith, K. A.; Smalley, R. E. *Chem. Phys. Lett.* **1999**, 313, 91.
- (5) Kitiyanan, B.; Alvarez, W. E.; Harwell, J. H.; Resasco, D. E. *Chem. Phys. Lett.* **2000**, 317, 497.
- (6) Bachilo, S. M.; Strano, M. S.; Kittrell, C.; Hauge, R. H.; Smalley, R. E.; Weisman, R. B. *Science* **2002**, 298, 2361.
- (7) Saito, R.; Dresselhaus, G.; Dresselhaus, M. S. *Physical Properties of Carbon Nanotubes*; Imperial College Press: London, 1998.
- (8) Strano, M. S.; Dyke, C. A.; Usrey, M. L.; Barone, P. W.; Allen, M. J.; Shan, H.; Kittrell, C.; Hauge, R. H.; Tour, J. M.; Smalley, R. E. *Science* **2003**, 301, 1519.
- (9) Dyke, C. A.; Stewart, M. P.; Tour, J. M. *J. Am. Chem. Soc.* **2005**, 127, 4497.
- (10) Collins, P. G.; Arnold, M. S.; Avouris, P. *Science* **2001**, 292, 706.
- (11) Chattopadhyay, D.; Galeska, I.; Papadimitrakopoulos, F. *J. Am. Chem. Soc.* **2003**, 125, 3370.



- (12) Kimura, S.; Kanda, M.; Hirashima, Y.; Hasegawa, T.; Wakahara, T.; Lian, Y.; Nakahodo, T.; Tsuchiya, T.; Akasaka, T.; Lu, J.; Zhang, X.; Gao, Z.; Yu, Y.; Nagase, S.; Kazaoui, S.; Minami, N.; Shimizu, T.; Tokumoto, H.; Saito, R. *J. Am. Chem. Soc.* **2005**, *127*, 10287.
- (13) Zheng, M.; Jagota, A.; Strano, M. S.; Santos, A. P.; Barone, P.; Chou, S. G.; Diner, B. A.; Dresselhaus, M. S.; Mclean, R. S.; Onoa, G. B.; Samsonidze, G. G.; Semke, E. D.; Usrey, M.; Walls, D. J. *Science* **2003**, *302*, 1545.
- (14) Doorn, S. K.; Strano, M. S.; O'Connell, M. J.; Haroz, E. H.; Rialon, K. L.; Hauge, R. H.; Smalley, R. E. *J. Phys. Chem. B* **2003**, *107*, 6063.
- (15) Heller, D. A.; Mayrhofer, R. M.; Baik, S.; Grinkova, Y. V.; Usrey, M. L.; Strano, M. S. *J. Am. Chem. Soc.* **2004**, *126*, 14567.
- (16) Krupke, R.; Hennrich, F.; Lohneysen, H.; Kappes, M. M. *Science* **2003**, *301*, 344.
- (17) Krupke, R.; Hennrich, F.; Kappes, M. M.; Lohneysen, H. *Nano Lett.* **2004**, *4*, 1395.
- (18) Kim, Y.; Hong, S.; Jung, S.; Strano, M. S.; Choi, J.; Baik, S. J. *Phys. Chem. B* **2006**, *110*, 1541.
- (19) Blatt, S.; Hennrich, F.; Lohneysen, H.; Kappes, M. M.; Vijayaraghavan, A.; Krupke, R. *Nano Lett.* **2007**, *7*, 1960.
- (20) Dimaki, M.; Boggild, P. *Nanotechnology* **2004**, *15*, 1095.
- (21) Kim, J.; Han, C. *Nanotechnology* **2005**, *16*, 2245.
- (22) Arnold, M. S.; Green, A. A.; Hulvat, J. F.; Stupp, S. I.; Hersam, M. C. *Nature Nanotech.* **2006**, *1*, 60.
- (23) Peng, H.; Alvarez, N. T.; Kittrell, C.; Hauge, R. H.; Schmidt, H. K. *J. Am. Chem. Soc.* **2006**, *128*, 8396.
- (24) Pohl, H. A. *J. Appl. Phys.* **1958**, *29*, 1182.
- (25) Diehl, M. R.; Yaliraki, S. N.; Beckman, R. A.; Barahona, M.; Heath, J. R. *Angew. Chem., Int. Ed.* **2002**, *41*, 353.
- (26) Huang, Y.; Wang, X.; Becker, F. F.; Gascoyne, P. R. *Biophys. J.* **1997**, *73*, 1118.
- (27) Hobbie, E. K. *J. Chem. Phys.* **2004**, *121*, 1029.
- (28) Bohren, C. F.; Huffman, D. R. *Absorption and Scattering of Light by Small Particles*; Wiley-VCH: New York, 1983.
- (29) Jones, T. B. *Electromechanics of Particles*; Cambridge University Press: Cambridge, 1995.
- (30) Jeon, T.; Kim, K.; Kang, C.; Oh, S.; Son, J.; An, K. H.; Bae, D. J.; Lee, Y. H. *Appl. Phys. Lett.* **2002**, *80*, 3403.
- (31) Fagan, J. A.; Simpson, J. R.; Landi, B. J.; Richter, L. J.; Mandelbaum, I.; Bajpai, V.; Ho, D. L.; Raffaele, R.; Walker, A. R.; Bauer, B. J.; Hobbie, E. K. *Phys. Rev. Lett.* **2007**, *98*, 147402.
- (32) Fagan, J. A.; Bajpai, V.; Bauer, B. J.; Hobbie, E. K. *Appl. Phys. Lett.* **2007**, *91*, 213105.
- (33) Ugawa, A.; Rinzler, A. G.; Tanner, D. B. *Phys. Rev. B: Condens. Matter Mater. Phys.* **1999**, *60*, R11305.
- (34) Hilt, O.; Brom, H. B.; Ahlskog, M. *Phys. Rev. B: Condens. Matter Mater. Phys.* **2000**, *61*, R5129.
- (35) Hao, J.; Hanson, G. W. *IEEE Trans. Nanotechnol.* **2006**, *5*, 766.
- (36) Burke, P. J.; Li, S.; Yu, Z. *IEEE Trans. Nanotechnol.* **2006**, *5*, 314.
- (37) O'Connell, M. J.; Bachilo, S. M.; Huffman, C. B.; Moore, V. C.; Strano, M. S.; Haroz, E. H.; Rialon, K. L.; Boul, P. J.; Noon, W. H.; Kittrell, C.; Ma, J.; Hauge, R. H.; Weisman, R. B.; Smalley, R. E. *Science* **2002**, *297*, 593.
- (38) Mureau, N.; Mendoza, E.; Silva, S. R.; Hoettges, K. F.; Hughesa, M. P. *Appl. Phys. Lett.* **2006**, *88*, 243109.
- (39) Grassia, P. S. *J. Fluid Mech.* **1995**, *282*, 373.
- (40) Doi, M.; Edwards, S. F. *The Theory of Polymer Dynamics*; Oxford Science Publications: New York, 1986.
- (41) Ottinger, H. C. *Stochastic Processes in Polymeric Fluids*; Springer: Berlin, 1996.
- (42) Duggal, R.; Pasquali, M. *Phys. Rev. Lett.* **2006**, *96*, 246104.
- (43) Parra-Vasquez, A. N.; Stepanek, I.; Davis, V. A.; Moore, V. C.; Haroz, E. H.; Shaver, J.; Hauge, R. H.; Smalley, R. E.; Pasquali, M. *Macromolecules* **2007**, *40*, 4043.
- (44) Shaikh, F. A.; Ugaz, V. M. *Proc. Natl. Acad. Sci. U.S.A.* **2006**, *103*, 4825.
- (45) Neipp, C.; Hernandez, A.; Belendez, T.; Rodes, J. J.; Belendez, A. *Am. J. Phys.* **2003**, *71*, 46.
- (46) Wang, S.; Liang, Z.; Wang, B.; Zhang, C. *Nanotechnology* **2006**, *17*, 634.
- (47) Carver, R. L.; Peng, H.; Sadana, A. K.; Nikolaev, P.; Arepalli, S.; Scott, C. D.; Billups, W. E.; Hauge, R. H.; Smalley, R. E. *J. Nanosci. Nanotechnol.* **2005**, *5*, 1035.
- (48) Becker, M. L.; Fagan, J. A.; Gallant, N. D.; Bauer, B. J.; Bajpai, V.; Hobbie, E. K.; Lacerda, S. H.; Migler, K. B.; Jakupciak, J. P. *Adv. Mater.* **2007**, *19*, 939.
- (49) Yang, Y.; Xie, L.; Chen, Z.; Liu, M.; Zhu, T.; Liu, Z. *Synth. Met.* **2005**, *155*, 455.
- (50) Benedict, L. X.; Louie, S. G.; Cohen, M. L. *Phys. Rev. B: Condens. Matter Mater. Phys.* **1995**, *52*, 8541.
- (51) Nelder, J. A.; Mead, R. *Comput. J.* **1965**, *7*, 308.
- (52) Lagarias, J. C.; Reeds, J. A.; Wright, M. H.; Wright, P. E. *SIAM J. Optim.* **1998**, *9*, 112.
- (53) Hitt, D. L.; Macken, N. *Trans. ASME* **2004**, *126*, 758.